Site-specific X-ray photoelectron spectroscopy using X-ray standing waves

J.C. Woicik

National Institute of Standards and Technology, Gaithersburg, MD 20899, USA

Available online 9 June 2005

Abstract

We describe how X-ray photoelectron spectroscopy (XPS) measurements when conjoined with dynamical X-ray Bragg diffraction can determine site-specific electronic structure information. This result depends on the dipole approximation for the valence photo-excitation process in the low-energy X-ray limit that we validate through angle-integrated X-ray standing-wave (XSW) measurements of single-crystal Cu. We demonstrate the site-specific XPS technique for the single-crystal rutile TiO_2 valence band and extract the individual Ti and O photoelectron partial density of states. First principles density functional calculations agree with our data after the angular-momentum-dependent photo-ionization cross-sections are properly accounted for.
Published by Elsevier B.V.

PACS: 68.49.Uv; 79.60.−i; 71.15.Mb

Keywords: X-ray standing waves; Electronic structure

X-ray photoelectron spectroscopy (XPS) has emerged as the premiere method to study the electronic structure of solids and films. The technique is based on the conservation of energy between the incoming photons and the outgoing photoelectrons as described by Einstein:

$$E_{kin} = \hbar\omega - E_b, \qquad (1)$$

where E_b is the binding energy of the electron in the solid, E_{kin} is the kinetic energy of the photoelectron in the vacuum that is determined by its final-state wave vector $\mathbf{k}_f$ ($E_{kin} = \hbar k_f^2/2m$), and $\hbar\omega$ is the photon energy. Consequently, an XPS experiment is conducted by impinging a sample with monochromatic photons and energy analyzing the resulting photoelectron spectrum. In this way, the electronic structure of a material may be determined uniquely [1].

Traditional synchrotron-based photoelectron spectroscopy experiments are performed using ultra-violet photons in the low-photon-energy range of 10–200 eV. As low-energy photoelectrons are extremely surface sensitive, the general application of the technique has been limited to the

near-surface region of materials. Clearly, there is a materials' science driven need to extend the kinetic-energy range of these experiments to the higher-energy X-rays. The resulting tunability of the photoelectron inelastic mean-free path will allow matching the depth sensitivity of photoelectron spectroscopy to real materials' science problems, such as layered materials and buried interfaces. Additionally, the larger photon-energy range of X-ray synchrotron beamlines will give access to deeper bound core levels making it possible to collect both bulk and surface sensitive chemical-state information from the same element within a material. Synchrotron-based X-ray photoelectron spectroscopy experiments should therefore mitigate the fixed-depth probing problem of conventional laboratory X-ray sources that arises due to the fixed-energy of both the source and core level.

The use of X-ray photons also opens the possibility of combining photoelectron spectroscopy with other well-established X-ray techniques, such as X-ray diffraction. In particular, because photoelectron spectroscopy measurements are performed with X-ray excitation sources that are (at best) monochromatic plane waves, the technique itself possesses no spatial sensitivity on the length scale of the crystalline-unit cell. Here we describe how XPS measurements when conjoined with dynamical X-ray Bragg diffraction can determine site-specific electronic structure information. The resulting site-specific XPS spectra may be used to test both the predictive power and accuracy of theoretical calculations that model solid-state electronic structure.

Under the condition of strong X-ray Bragg diffraction, the spatial dependence of the electric field is given by the superposition of the incident $\mathbf{E}_0$ and reflected $\mathbf{E}_h$ X-ray beams that travel with wave vectors $\mathbf{k}_0$ and $\mathbf{k}_h$, polarization vectors $\boldsymbol{\varepsilon}_0$ and $\boldsymbol{\varepsilon}_h$, and frequency ω:

$$\mathbf{E}(\mathbf{r}, t) = [\boldsymbol{\varepsilon}_0 E_0 e^{i\mathbf{k}_0 \cdot \mathbf{r}} + \boldsymbol{\varepsilon}_h E_h e^{i\mathbf{k}_h \cdot \mathbf{r}}]e^{-i\omega t}. \quad (2)$$

$\mathbf{k}_0$ and $\mathbf{k}_h$ are connected by the Bragg condition $\mathbf{h} = \mathbf{k}_h - \mathbf{k}_0$, where $\mathbf{h}$ is a reciprocal-lattice vector of the crystal. For the σ-polarization of a symmetric reflection, this field squares to give the electric-field intensity at the point $\mathbf{r}$ in space:

$$I(\mathbf{r}) = |E_0|^2[1 + R + 2\sqrt{R}\cos(v - \mathbf{h} \cdot \mathbf{r})]. \quad (3)$$

In this equation, v is the phase of the complex-field amplitude ratio $E_h/E_0 = \sqrt{R} \cdot e^{iv}$, and R is the reflectivity $R = |E_h/E_0|^2$. Germane to the site-specific XPS technique is the unique ability to position the maxima or minima of the electric-field intensity at any position within the crystalline-unit cell by varying the phase of the complex reflectivity between $0 < v < \pi$. This is achieved experimentally as shown in Fig. 1 by varying either the sample angle or the photon-energy within the natural width of the crystal X-ray Bragg diffraction [2].

Fig. 2 compares the photon-energy dependence of the Cu-3p core and Cu-valence photoelectron intensity near the Cu(11$\bar{1}$) Bragg back-reflection condition that occurs at $\hbar\omega \sim 2974$ eV [3]. These XSW photoelectron-emission patterns have been recorded in a fixed-angle, normal-incidence diffraction geometry by scanning the photon-energy across the Bragg condition and setting the energy window of the hemispherical electron analyzer to collect either the Cu-3p core or the Cu-valence band photoelectron emission. The curves have been scaled only by a constant to make equal their intensities away from the Bragg condition.

The yields from the core and valence electrons are strikingly similar, with the valence photoelectron emission showing only a small ($\sim$5%) reduction in XSW amplitude relative to the core emission. Due to the extreme spatial sensitivity of the XSW technique, it is clear that nearly all ($\sim$95%) of the Cu-valence photoelectron emission originates from the same localized emission volume as the Cu-3p core electrons. This result is surprising due to the large amount of valence charge that resides between the cores, and it demonstrates that this interstitial region of delocalized valence charge is transparent to the X-rays; i.e., only the core region of the valence-wave function contributes to the photo-excitation process.

In order to ascertain whether all the different energy states of the crystal-valence band have this same behavior, we collected high-resolution Cu valence-photoelectron spectra at different photon energies throughout the Cu(11$\bar{1}$) X-ray rocking

X-ray standing Waves
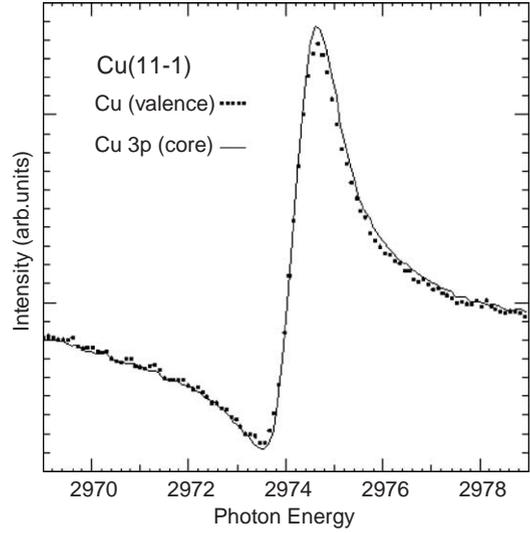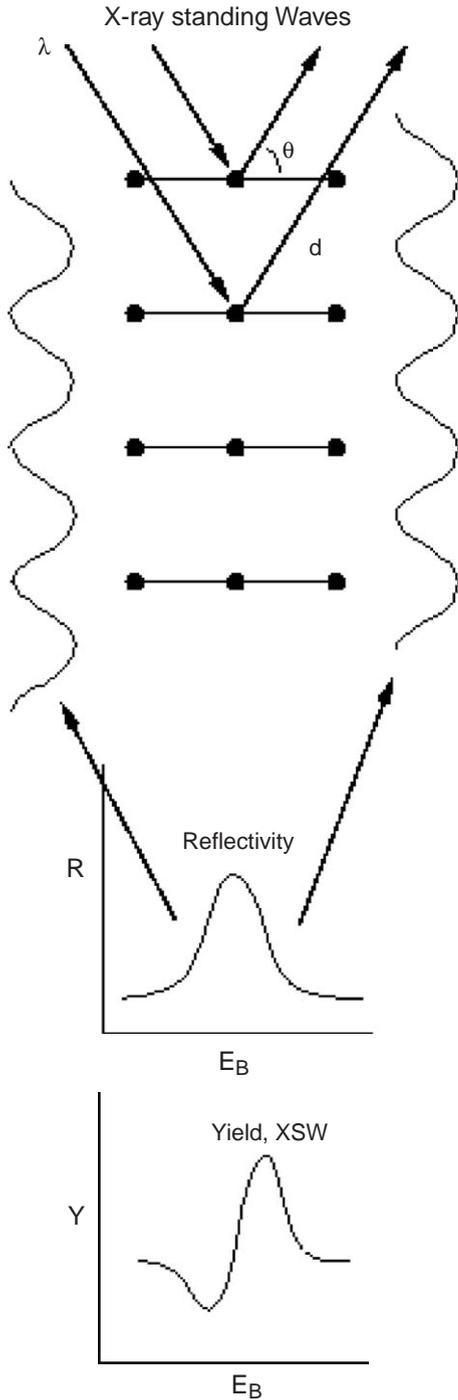
Fig. 2. Photon-energy dependence of the Cu 3p core (solid line) and the Cu valence photoelectron emission (dots) near the Cu(11$\bar{1}$) Bragg back-reflection condition.

curve. These spectra are shown in Fig. 3. They have been recorded with the XSW-intensity maxima placed on the Cu atoms, between the Cu atoms, intermediate to these two extremes, and 5 eV below the Bragg condition where the electric-field intensity is constant throughout the Cu unit cell. The modulation in yield and shift in energy across the Cu rocking curve are evident. Fig. 4 plots these spectra relative to the Fermi energy and normalized to equal intensity [3]. Remarkably, they are indistinguishable. All Cu-valence states, including the most delocalized states at the Fermi energy, must therefore have the same approximate linear response to the XSW-electric-field intensity at the location of the core.

In order to understand the physics behind this result, we apply Fermi's golden rule that gives the intensity of the photo-excitation process as the

Fig. 1. Diagram representing the XSW technique. At the low-energy side of the reflectivity, the maxima of the XSW-interference field are between the atomic planes of the crystal, whereas at the high-energy side the maxima are on the atomic planes. The suppression and enhancement of the photoyield is evident.
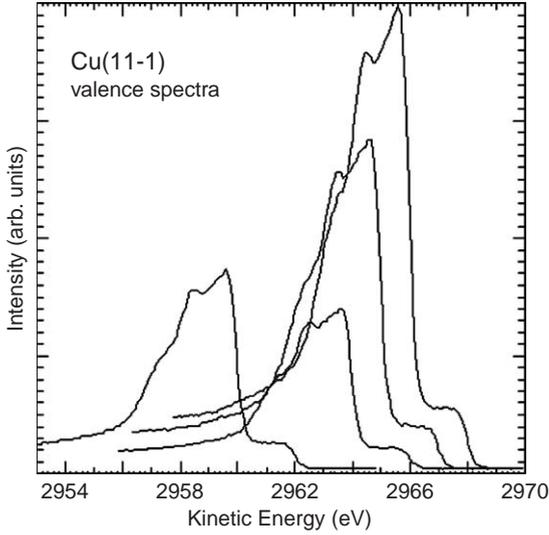
Fig. 3. High-resolution Cu valence photoelectron spectra recorded at different photon energies within the natural width of the Cu(11$\bar{1}$) Bragg back reflection and 5 eV below the Bragg condition.
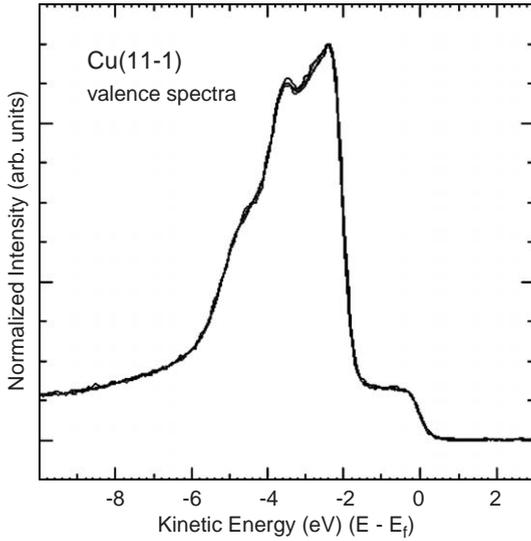
Fig. 4. Comparison of the high-resolution Cu valence photoelectron spectra from Fig. 3. The spectra have been normalized to equal height and referenced to the Fermi energy.

square modulus of the transition-matrix element M_{if} between the initial and final states:

$$d\sigma/d\Omega \propto |M_{if}|^2, \tag{4}$$

where $M_{if} = \langle f | E_0 e^{i\mathbf{k}_0 \cdot \mathbf{r}}(\varepsilon_0 \cdot \mathbf{p}) | i \rangle$. In a single-particle approximation, $|i\rangle$ is the initial, bound-state wave function of the electron in the ground state of the Hamiltonian $H_0 = \Sigma_i p_i^2/2m + V(\mathbf{r})$, and $|f\rangle$ is the final, continuum-state wave function of the photoelectron in the vacuum. $\mathbf{k}_0$ is the wave vector of the time-dependent perturbing photon field ($H' = \mathbf{A}_0 \cdot \mathbf{p}$), $V(\mathbf{r})$ is the crystal potential, and $\mathbf{p} = -i\hbar\nabla$, is the momentum operator.

As the binding energy of a valence electron is negligible ($E_b \ll \hbar\omega$), we may treat the final-state wave function as an energetic plane wave in the Born approximation: $|f\rangle = e^{i\mathbf{k}_f \cdot \mathbf{r}}$ [4]. Because the photon-wave vector at the low X-ray energies is much smaller than the final-state wave vector of the photoelectron ($k_0 \ll k_f$), the photon-wave vector will make a negligible contribution to the matrix element. (Although this situation is not true in general, it is expected to be valid as long as $\hbar\omega \ll mc^2$ [5]). This result is equivalent to the dipole approximation ($\mathbf{k}_0 \cdot \mathbf{r} = 0$), and it demonstrates that the intensity of the valence emission is proportional to the electric-field intensity at the location of the core, despite the large spatial extent of the valence wave function.

To understand the observed localization of the emitter volume, we may use the commutator $[\mathbf{p}, H] = -i\hbar\nabla V(\mathbf{r})$ together with the dipole approximation and the fact that both $|i\rangle$ and $|f\rangle$ are eigenstates of H_0 to re-write M_{if} in terms of the gradient of the potential:

$$M_{if} = \langle f | \varepsilon_0 \cdot \nabla V(\mathbf{r}) | i \rangle. \tag{5}$$

This equation is the "dipole acceleration" form of the matrix element [6]. It is analogous to the classical force acting on an electron ($\mathbf{F} = -\nabla V(\mathbf{r})$), and it demonstrates that photoelectron emission occurs only from the spatial region of the crystal where the crystal potential is rapidly changing. For a typical crystal potential, this situation is realized only in the immediate vicinity of the core. Consequently, it is the high kinetic energy of the emitted photoelectron in the low energy X-ray limit [7] that leads to the equivalence of the core and valence XSW-emission patterns of Fig. 2 and the insensitivity of the valence line shape of Fig. 3 to the placement of the XSW-interference field within the Cu unit cell.
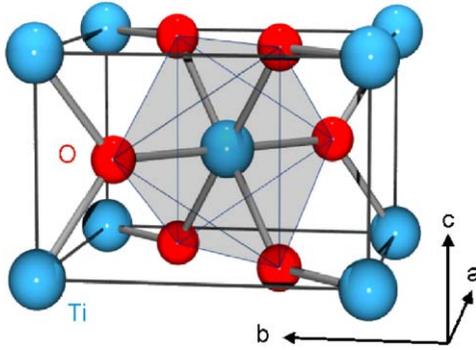
Fig. 5. Crystal structure of rutile TiO_2.

Fig. 6. Photoelectron spectra from rutile TiO_2 recorded at two different photon energies within the photon-energy width of the $TiO_2(2\,0\,0)$ Bragg back reflection. The photon energies were chosen to maximize the XSW electric-field intensity on either the Ti (solid curve) or O (dotted curve) atomic planes.

Having addressed the valence-electron emission of Cu under XSW excitation, we now turn to the non-trivial example of the site-specific XPS spectra of the ionic crystal rutile TiO_2. Fig. 5 shows the rutile crystal structure. The rutile unit cell contains two Ti atoms and four O atoms. Six O ligands surround each Ti atom in a slightly distorted octahedron. Ti has the ground-state electronic configuration $3d^2 4s^2$, and simple electron counting finds the formal ionization state of Ti in TiO_2 to be Ti^{4+}, giving the O atoms a $2p^6$ closed-shell atomic configuration.

Fig. 6 shows the resulting photoelectron "on site" spectra from the TiO_2 (1 1 0) surface [8]. These spectra have been recorded at two different photon energies within the photon-energy width of the rutile TiO_2 (2 0 0) Bragg back-reflection condition that occurs at $\hbar\omega \sim 2700\,eV$. These photon energies were chosen to place the maxima of the electric-field intensity on either the Ti or O atomic planes. Note the relative change in intensity of the Ti and O core lines as well as the crystal-valence band with placement of the XSW-interference field.

From our validation of the dipole approximation, it is clear that the valence photoelectron emission appears as the sum of the individual Ti and O components of the TiO_2 valence band weighted by the electric-field intensities at the Ti and O core sites. Consequently, the individual Ti and O components of the valence band may be obtained by taking the appropriate linear combinations of the "on site" spectra normalized to

the relative intensity of the Ti 3p and O 2s core lines [9]. The resulting site-specific Ti and O photoelectron partial density of states are shown in Fig. 7 [8].

The large contribution of Ti to the valence-band spectrum indicates significant covalent bonding between the Ti and O atoms, despite the formal Ti^{4+} charge state of Ti in rutile. (Had the Ti atoms been completely ionized, there would be no Ti valence-electron emission). These spectra are compared to theoretical Ti and O partial density of states curves that were calculated using the local density approximation within density functional theory [8].

The electronic structure of the first-row transition-metal oxides is based on the chemical bonding between the metal 3d, 4s, and 4p states and the oxygen 2s and 2p states in octahedral symmetry [10]. From molecular-orbital theory, the metal 4s orbitals bond with the ligand σ orbitals to form the $a_{1g}(\sigma^b)$ level, the metal $3d_{x2-y2}$ and $3d_{z2}$ orbitals bond with the ligand σ orbitals to form the $e_g(\sigma^b)$ level, the metal 4p orbitals bond with both the ligand σ and π orbitals to form the $t_{1u}(\sigma^b)$ and $t_{1u}(\pi^b)$ levels, and the metal $3d_{xy}$, $3d_{xz}$, and $3d_{yz}$ orbitals bond with the ligand π orbitals to
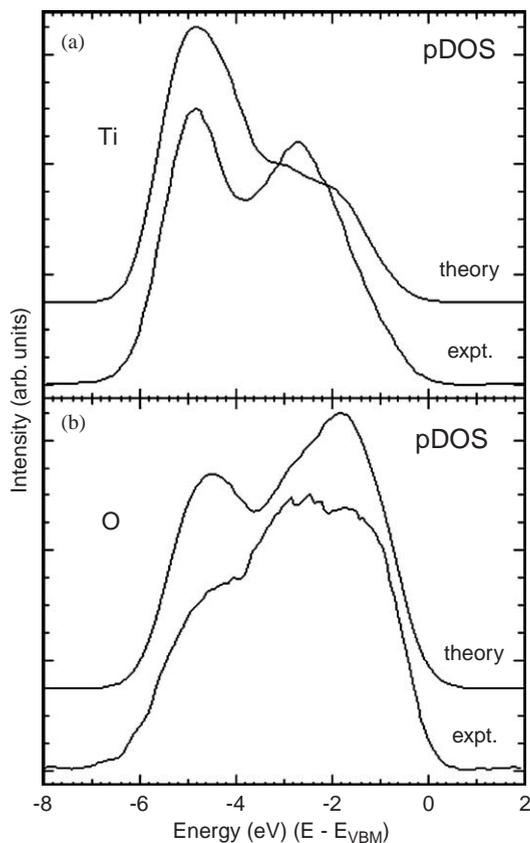
Fig. 7. Experimental site-specific XPS valence photoelectron spectra and theoretical partial density of states: (a) Ti; (b) O. The curves have been scaled to equal peak height. The O component has been scaled by a factor of 4 relative to the Ti component.

Fig. 8. Different angular-momentum components of the theoretical Ti and O partial density of states. Multipliers relative to the O 2p component are indicated in each case.

form the $t_{2g}(\pi^b)$ level. Additionally, there are ligand π orbitals [$t_{1g}(\pi)$ and $t_{2u}(\pi)$] that are left over and are rigorously non-bonding in O_h symmetry.

Examination of the experimental site-specific XPS spectra leads to an attractive interpretation of the electronic structure of rutile TiO_2 within this σ and π bonding scheme. The doubly lobed Ti structure may be attributed to the energy splitting between the σ and π groupings of the bonding states, with the σ states lying at the lower energy. These states are mirrored in the triply peaked O structure, indicating the sharing of electrons in a covalent bond. The O non-bonding π states naturally compose the third lobe of the O

spectrum; they occur at higher energy than the O bonding π states and have little or no electron density on the Ti atoms as expected. Because the last occupied electronic states of this ionic crystal reside on the anion sites, it is clear why rutile TiO_2 is an insulator.

Drawing on this physical insight, the theoretical Ti and O partial density of states were decomposed into their angular momentum resolved components. These curves are shown in Fig. 8 [8]. It is clear that the second lobe of the experimental Ti spectrum cannot be reproduced without the inclusion of the Ti 4p component, and the second peak of the experimental O spectrum cannot be reproduced without inclusion of the O 2s component.

Because the photo-excitation process conserves angular momentum [5], we modeled the theoretical partial density of states curves from the weighted sums of the different orbital components of Fig. 8 using the tabulated theoretical atomic cross sections: Ti $\sigma_{4s}/\sigma_{3d} \sim 9.9$ and O $\sigma_{2s}/\sigma_{2p} \sim 29$ [11]. Agreement between the theoretical and experimental partial density of states was much improved; however, even better agreement was obtained for both the Ti and O components when the relative atomic cross sections were scaled by an additional factor of 2. A full 1.5 of this factor of 2 could come from the choice of theoretical deconvolution radii used in the calculation of the individual components (the covalent radii of Ti and O were used), in addition to changes in the theoretical cross sections in going from the atomic to the solid state [12]. The resulting theoretical corrected partial density of states are shown in Fig. 9 together with the experimental data [8]. Agreement now between theory and experiment is startling, and this agreement has been achieved without any energy dependence of the cross sections across the energy width of the valence band or the consideration of many-body effects.

At this point it is instructive to examine the hybridization of the metal and ligand atoms more closely. As both the O 2s and O $2p_z$ atomic orbitals belong to the same symmetry representation of the O_h point group, the ligand σ orbitals will always contain a mixture of these states [10]: $|\psi_{L,\sigma}\rangle = \alpha|2s> + \sqrt{(1-\alpha^2)}|2p_z\rangle$. (The ligand π orbitals are constructed solely from the O $2p_x$ and O $2p_y$ atomic orbitals.) This hybridization orients the ligand-charge density towards the metal atoms, leading to an increased overlap between the metal and ligand wave functions. It has been stated by Mulliken that "a little hybridization goes a long way" to stabilize a chemical bond [10]. From the theoretical calculations of Fig. 8, we see that α, the mixing coefficient, is only $\sim 10\%$ (electron density is $\psi^*\psi$), even though the O 2s valence (or hybrid) component accounts for as much as $\sim 30\%$ of the experimental O valence spectrum due to the much larger crosssection of the O 2s versus the O 2p atomic orbitals. This relatively small value of α results from the relatively large energy separation be-
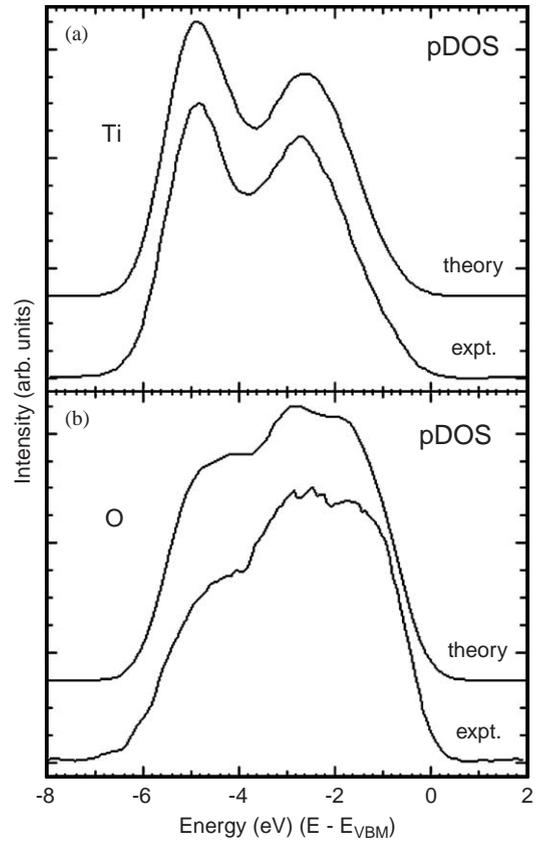
Fig. 9. Experimental site-specific XPS valence photoelectron spectra and theoretical partial density of states. The theoretical partial density of states have been corrected for the individual angular-momentum dependent photo-ionization crosssections: (a) Ti; (b) O. The curves have been scaled to equal peak height.

tween the O 2s and O 2p atomic orbitals that is $\sim 17\,eV$, as seen from Fig. 6. On the other hand, the energy separation between the Ti 3d, 4s, and 4p atomic orbitals is significantly smaller, $\sim 8\,eV$ [13], accounting for the much larger amount of hybridization observed on the metal site.

Amusingly, it is the added complexity of the photo-excitation process; i.e., the "over representation" of orbitals with smaller values of angular momenta (O 2s versus O 2p and Ti 4s and 4p versus Ti 3d) that affords this direct observation of chemical hybridization in the solid state: the observation of σ and π bonds and of oxygen nonbonding states, and the positive identification of valence-band contributions from the O 2s and Ti

4s and 4p orbitals. Had these components not been properly taken into account, then the poor agreement between theory and experiment of Fig. 7 would have provoked the erroneous conclusion that the theoretical calculations fail to predict accurately the electronic structure of rutile TiO_2.

In conclusion, we have demonstrated that X-ray photoelectron spectroscopy when conjoined with dynamical X-ray Bragg diffraction can determine the site-specific chemical components of a crystal valence band experimentally. The technique is ideally suited for studying chemical hybridization in the solid state and for testing both the predictive power and accuracy of theoretical calculations that model solid-state electronic structure while emphasizing the importance of the individual angular-momentum components of the crystal potential in valence-photoelectron spectra. It should also be applicable to core-level studies of crystalline materials with multi-atom unit cells and impurity atoms with different oxidation states. Unlike traditional XPS measurements, the site-specific XPS technique uniquely reveals the genealogy of the solid-state chemical bond.

References

[1] S. Hufner, Photoelectron Spectroscopy: Principles and Applications, 2nd ed, Springer, Berlin, 1996.

[2] B.W. Batterman, H. Cole, Rev. Mod. Phys. 36 (1964) 681.

[3] J.C. Woicik, E.J. Nelson, D. Heskett, J. Warner, L.E. Berman, B.A. Karlin, I.A. Vartanyants, M.Z. Hasan, T. Kendelewicz, Z.X. Shen, P. Pianetta, Phys. Rev. B 64 (2001) 125115.

[4] The Born approximation may not be valid in the core region; however, close to the core $\mathbf{k}_0 \cdot \mathbf{r} \sim 0$, and the standard description of the dipole approximation applies.

[5] H.A. Bethe, E.E. Salpeter, Quantum Mechanics of One- and Two-Electron Atoms, Plenum, New York, 1977 Chapter 4.

[6] I. Adawi, Phys. Rev. B 134 (1964) A788.

[7] J.C. Woicik, E.J. Nelson, P. Pianetta, Phys. Rev. Lett. 84 (2000) 773.

[8] J.C. Woicik, E.J. Nelson, L. Kronik, M. Jain, J.R. Chelikowsky, D. Heskett, L.E. Berman, G.S. Herman, Phys. Rev. Lett. 89 (2002) 077401.

[9] J.C. Woicik, E.J. Nelson, T. Kendelewicz, P. Pianetta, Phys. Rev. B 63 (2001) 041403(R).

[10] C.J. Ballhausen, H.B. Gray, Molecular Orbital Theory, Benjamin, New York, 1964 Chapters. 4 and 8.

[11] M.B. Trzhaskovskaya, V.I. Nefedov, V.G. Yarzhemsky, At. Data Nucl. Data Tables 77 (2001) 97.

[12] For example, the theoretical calculations of the Ti atomic cross sections were performed for the ground state Ti $4s^2 3d^2$ atom [11]. The occupation of the Ti 4p orbital found here corresponds to an excited state of the atomic system.

[13] Z. Zhang, S.-P. Jeng, V.E. Henrich, Phys. Rev. B 43 (1991) 12004.